HOKKAIDO UNIVERSITY

Title	Low- and High-Density Unknown Waters at Ice-Water Interfaces
Author(s)	Niinomi, Hiromasa; Kouch, Akira; Hama, Tetsuya; Nada, Hiroki; Yamazaki, Tomoya; Kimura, Yuki
Citation	Journal of physical chemistry letters, 13(19), 4251-4256 https://doi.org/10.1021/acs.jpclett.2c00660
Issue Date	2022-05-11
Doc URL	http://hdl.handle.net/2115/89200
Rights	This document is the Accepted Manuscript version of a Published Work that appeared in final form in The Journal of Physical Chemistry Letters, copyright © American Chemical Society after peer review and technical editing by the publisher. To access the final edited and published work see https://pubs.acs.org/articlesonrequest/AOR-RR3TNCITDDRE3HJ2IKDH.
Type	article (author version)
Additional Information	There are other files related to this item in HUSCAP. Check the above URL.
File Information	Niinomi_et_al_JPCL_SI.pdf (Supporting Information)

Supporting Information for

Low- and High-Density Unknown Waters at Ice–Water Interfaces

Hiromasa Niinomi*[†,‡], Akira Kouch[†], Tetsuya Hama[§], Hiroki Nada[¶], Tomoya Yamzaki[†] and Yuki Kimura*[†]

[†] Institute of Low Temperature Science, Hokkaido University, Kita-19, Nishi-8, Kita-ku, Sapporo, 060-0819, Japan
[‡] Institute of Multidisciplinary Research for Advanced Materials, Tohoku University, 2-1-1 Katahira, Aoba-ku, Sendai, 980-8577, Japan
[§] Komaba Institute for Science, the University of Tokyo, 3-8-1 Komaba, Meguro, Tokyo 153-8902, Japan
[¶] National Institute of Advanced Industrial Science and Technology (AIST), 16-1 Onogawa, Tsukuba 305-8569, Japan

Corresponding authors: Hiromasa Niinomi (HN), Yuki Kimura (YK)
Email: hiromasa.niinomi.b2@tohoku.ac.jp (HN), ykimura@lowtem.hokudai.ac.jp (YK)

This PDF file includes:

Other supporting materials for this manuscript include the following:

SI Movies S1 to S5

Supporting Information Text S1

The details of experimental methods.

In the sapphire anvil cell (SAC), three piezo actuators (N 20/S 10, P-232-40; Piezosystem Jena GmbH, Jena, Germany) were embedded between stainless steel sheets supporting a pair of sapphire anvils in a symmetrical arrangement (SEED; Syntek Co. Ltd, Yokohama, Japan). The SAC was also equipped with a manual pressure-adjustment system using a screw (Figure S1). This design permitted dynamic and fine control of (de)pressurization by electrically actuating the piezo elements with a piezo amplifier (E-662; PI, Auburn, MA, USA) connected to a function generator (33522B; Keysight, Santa Rosa, CA, USA), in addition to coarse adjustment by using the pressure-adjusting screw. Because this design concept was previously introduced by Evans *et al.* as the 'dynamic diamond anvil cell (d-DAC)'[22], we refer to our designed SAC as the dynamic SAC (d-SAC). Ultrapure water from an ultrapure-water-producing apparatus (Simplicity UV; Merck Millipore, Burlington, MA, USA) fed with distilled water (Kyoei Seiyaku Co., Tokyo, Japan) was used as the mother liquid for crystallization of ice I_h. Ice I_h was crystallized by keeping the d-SAC with the ultrapure water in its sample chamber without pressurization in a low-temperature room maintained at –10 °C. After crystallization of ice I_h, the ice crystals were melted by compression in the d-SAC; the pressure was controlled by using the coarse pressure adjustment to the pressure conditions for the coexistence of water and ice I_h (~107 MPa). Then, the crystals were repeatedly melted and grown by compression and decompression with the coarse adjuster, so that eventually only a single crystal remained in the sample chamber. A water–ice I_h interface was produced by growing the single crystal so as not to completely crystallize the coexisting water in the sample chamber. After the production of the water–ice interface, the ice I_h crystal was repeatedly grown and melted by depressurization/pressurization through fine adjustment by the piezo actuators. The piezo elements were actuated by applying square-wave voltages from the function generator. The frequencies and the peak-to-peak voltages for the square waves from the function generator were 125, 250, 400, and 500 mHz and 0.5, 1, 2, 3, 4, 5, 6, and 7 V_{pp}, respectively. The voltage was applied to the piezo actuators after a tenfold amplification by the amplifier. The interface between the water and the ice I_h crystal repeatedly grown and melted in synchronization with the applied square wave was observed *in situ* by bright-field microscopy, differential-interference phase-contrast microscopy, and Fizeau-type laser interferometric microscopy using an inverted optical microscope (IX71; Olympus Corp., Tokyo, Japan) located in the low-temperature room. The microscopic images were recorded *in situ* by using a CCD camera (UI-3180CP-C-HQ Rev.2; IDS Image Development Systems GmbH, Obersulm, Germany). The bright-field and differential-interference phase-contrast microscopy was conducted by using a set of commercially available optical components (Olympus Corp.). The laser interferometric microscope was constructed by combining a He–Ne laser (05-LHR-211; CVI Melles Griot, Albuquerque, NM, USA; λ = 632.8 nm) with the inverted optical microscope (Figure S2). The laser beam emitted in the horizontal direction was first introduced into an objective lens (SLMPLN20X; Olympus) and then passed to a polarization beam splitter (PBS) to introduce the laser light into the optical path of the inverted optical microscope by reflecting it in the vertical direction. The light reflected by the PBS was next introduced through an objective lens (SLMPLN20X; Olympus) for sample observation; this lens collimated the introduced light. The ice I_h crystal was irradiated by the collimated laser

beam, and the incident laser light and the light reflected by interfaces interfered with each other to produce interference fringes (Figure S2).

Supporting Information Text S2

Thermodynamic driving force for crystallization by d-SAC.

To obtain the effective thermodynamic driving force ($\Delta\mu$) for crystallization caused by an effective overdepression at the water–ice I_h interface imposed by applying a voltage to the piezo actuators in the d-SAC (see Materials and Methods), we investigated the relationship between the output voltage from function generator connected to the piezo actuators (V_{pp}) (See Materials and Methods) and the corresponding crystal-growth velocity. In a previous study, Kim *et al.* showed that the local overpressure at the interface required to drive the crystal growth of ice VI from water can be significantly larger than the global overpressure estimated simply from the pressure-induced change in volume of the sample chamber of a dynamic diamond anvil cell (d-DAC)[22,25]. They termed the local overpressure at the interface the 'effective overpressure'. Here, we also investigated the effective overpressure and the thermodynamic driving force at the interface. It is generally known in crystallization from a melt that the relationship between the crystal-growth velocity V and the thermodynamic driving force can be expressed as follows[25]:

$$V = V_0 \left[1 - \exp\left(-\frac{\Delta\mu}{k_B T}\right) \right] \qquad (S1)$$

where V_0 is the kinetic coefficient, k_B is the Boltzmann constant, T is the absolute temperature, and $\Delta\mu$ is the product of the overpressure ΔP and the volume change between the melt and the crystalline phase per molecule (Δv). Since Δv is constant, we can assume that ΔP is proportional to the output voltage from the function generator, namely, $\Delta P \propto \Delta\mu = \alpha V_{pp}$ where α is a constant. The growth velocity of ice I_h was measured by *in situ* bright-field observation of the dynamics of its crystal growth from water on actuating the d-SAC. Note that the overdepression was investigated in this case, because the crystallization of I_h from water is driven by depressurization. A single crystal of ice I_h was prepared in the sample chamber of the d-SAC by manual adjustment of the pressure-adjustment screw (See Supporting Information Text S1). Figure S3 **A** presents a series of time-lapse micrographs showing the crystal-growth dynamics of a prepared single crystal of ice driven by depressurization for output voltages (V_{pp}) of 1 and 5 V. The basal plane of the single crystal tended to develop into a disk-like rounded morphology, permitting easy measurement of the crystal-growth velocity in the lateral direction to the disk-like morphology. Figure S3 **B** shows the dependence of the crystal-growth velocity on the output voltage. The measured dependency, plotted as black circles, was well fitted by Eq. S1, meaning that the assumption that the thermodynamic driving force is proportional to the output voltage is feasible. The fitting of the dependency by using Eq. S1 allowed us to determine the value of the kinetic coefficient to be 9.982×10^{-5} and that of the constant α to be 1.225×10^{-21}. Therefore, the dependence of the effective overdepression at the interface and the thermodynamic driving force for crystallization on the output voltage can be obtained as shown in Figure S3 **C**. Note that the thermodynamic driving force that can be applied by a d-SAC is significantly higher than those achievable in supercooling experiments. For example, the driving force at $V_{pp} = 7$ V is about 8×10^{-21} J, which corresponds to the

driving force attained through supercooling by −219 °C. This degree of supercooling cannot be achieved experimentally, because the supercooling limit of water is about −46.15 °C, even for a water microdroplet floating in air[17]. This large thermodynamic driving force and overpressure at the interface might be important for generating unknown types of water.

Supporting Information Text S3
Estimation of the wetting angle of LDUW at the water–growing ice interface.
We estimated the wetting angle of the liquid thin layer of LDUW at the water–growing ice interface from its slope with respect to the ice surface by analysing the intervals between the interference fringes of the microinterferogram, on the assumption that the slope does not change at the contact line. As shown in Figure S4, the tangent of the wetting angle θ can be written as follows:

$$\tan \theta = \frac{d_2 - d_1}{L} \qquad \text{(S2)}$$

where d_1 and d_2 are the thickness of the LDUW thin layer at which the mth and the $(m + 1)^{\text{th}}$ constructive interference occurs (m is an integer) and L is the spatial interval between the mth and the $(m + 1)^{\text{th}}$ constructive interference fringes. The value of L can be obtained experimentally from the *in situ* interferogram. The value of d_2 and d_1 can be obtained from other expressions by considering the conditions for the mth and the $(m + 1)^{\text{th}}$ constructive interferences. These constructive interference conditions can be written as follows:

$$2n_L d_1 = m\lambda \qquad \text{(S3)}$$

$$2n_L d_2 = (m + 1)\lambda \qquad \text{(S4)}$$

where n_L is the refractive index of LDUW, λ is the wavelength of the laser light (λ = 632.8 nm). Subtraction of Eq. S3 from Eq. S4 gives the following relationship:

$$d_2 - d_1 = \frac{\lambda}{2n_L} \qquad \text{(S5)}$$

Therefore, tan θ, from which the value of θ can be deduced, can be obtained if the value of n_L is known. However, this is an unknown parameter. We therefore determined the possible range of values of θ by estimating the possible range of n_L. Because LDUW appears when the ice–water phase transformation occurs, its density is probably a value between that of ice and that of bulk water. Therefore, n_L should have a value between the refractive index of ice (n_I) and that of bulk water (n_W), that is $n_I < n_L < n_W$). Here the value of the refractive index of ice I_h at 1 atm (n_I = 1.31) was adopted as the minimum possible value of n_L, even though our observations were performed under a high pressure, because the refractive index of ice I_h increases with increasing applied pressure. On the other hand, the maximum possible value of n_L should be equal to the refractive index of bulk water at −10 °C and 107 MPa, the conditions for coexistence of water and ice I_h. To obtain the value of the refractive index of bulk water at −10 °C and 107 MPa, we referred to the dataset for the temperature–

pressure dependence of the refractive index provided by Cho *et al.*[38]. The temperature dependence at 1 atm is based on the Lorentz–Lorentz equation using a two-state formalism of water for its specific refraction[39], and this agrees with experimentally based values from the equation of Tilton and Taylor to within 1×10^{-5} or better for temperature from –10 to +70 °C[40].

We first obtained the refractive index of bulk water at –10 °C and 1 atm by extrapolating the temperature dependence for the range –5 to +5 °C for $\lambda = 501.568$ nm (as provided by Tilton and Taylor[40]) to –10 °C. The refractive index at –10 °C and 1 atm was calculated to be 1.33745, so that the value at −10 °C and 107 MPa could then be obtained, provided its pressure dependence at –10 °C could also be obtained. Cho *et al.* also determined the linear pressure dependences of the refractive index up to about 110 MPa at temperatures of 1.56, 7.64, 24.8, 34.5 and 54.34 °C for $\lambda = 643.847$ nm, as shown in Figure S5 **A**. The pressure dependence of the refractive index at several temperatures allowed us to determine the temperature dependence of the increment of the refractive index of bulk water per 0.1 MPa pressure increment (Δn_W), as shown in Figure S5 **B**. The value of Δn_W at –10 °C was obtained by extrapolating the resulting temperature dependence of Δn_W. From the calculated value of Δn_W at –10 °C, the refractive index of bulk water at –10 °C and 107 MPa was estimated to be about 1.35. Although a linear pressure dependence was assumed in estimating this value, this assumption is reasonable for estimating the maximum possible value of n_L, taking into account the fact that the experimentally measured pressure dependence of the refractive index of bulk water plateaus with the increment of pressure into consideration[41]. Therefore, the range of possible values of n_L was estimated to be $1.31 < n_L < 1.35$. This range, in conjunction with an analysis of the intervals of the interference fringes in the *in situ* interferogram to obtain the value of L, permitted the range of possible wetting angles to be estimated to be $1.76° < \theta < 1.82°$, as shown in the main text.

Supporting Information Text S4
Estimation of the maximum possible value for the viscosity of LDUW.
The maximum value of the viscosity of LDUW can be estimated by substituting the value of the interfacial tension between water and ice to the relationship $V^* = \gamma/\eta$, because the water–ice interfacial tension should be larger than the water–LDUW interfacial tension from the viewpoint of similarity of structure and bonding state. Previous studies have shown that the water–ice interfacial tension is probably in the range 20–32 mJ/m^2 [(42-44)] and an experimental measurement of the nucleation rate of small H_2O droplets found a value of 32.1 mJ/m^2 [(44)]. If we employ the value of 32.1 mJ/m^2 as the maximum value of the water–LDUW interfacial tension, the viscosity of the LDUW must be less than 1.6×10^{-3} Pa·s.

Supporting Information Text S5
Estimation of the viscosity of bulk water at –10 °C and 107 MPa.
The viscosity of bulk water at –10 °C and 107 MPa was estimated from the data for the temperature dependence of the viscosity of bulk water at 0.1 MPa provided by Dehaoui *et al.*[32] and the data for its pressure dependence at –10.35 °C provided by Singh *et al.*[31] (Figure S6). The pressure dependence presented in Figure S6 **A** shows that the ratio of the viscosity at a given temperature and pressure (in the range 0−360 MPa) to the viscosity at the given

temperature and a pressure of 0.1 MPa. The temperatures for which the pressure dependencies were provided were –28.85 °C (244.3 K), –27.85 °C (245.3 K), –25.35 °C (247.8 K), –20.35 °C (252.8 K), –15.35 °C (257.8 K), –10.35 °C (262.8 K), –5.35 °C (267.8 K), and 24.65 °C (297.8 K). We adopted the pressure dependence at –10.35 °C for our estimation. This pressure dependence allowed us to obtain a viscosity at –10 °C and 107 MPa, provided the viscosity at −10 °C and 0.1 MPa could be obtained. Fortunately, the viscosity at –10 °C and 0.1 MPa had been determined by Dehaoui *et al.*, as shown in Figure S6 **B**. As a result, we were able to estimate the viscosity of bulk water at –10 °C and 107 MPa to be about 2.3×10^{-3} Pa·s.

Supporting Information Text S6

Determination of the characteristic velocity of HDUW at the water–ice III interface.
Analysis of the nucleation-and-growth-type dewetting dynamics of a thin layer of HDUW permitted its characteristic velocity at the water–ice III interface to be determined (Figure S8). It is known that a thin film of liquid on a substrate with a negative spreading coefficient spontaneously dewets when the thickness of the thin film (e) falls below a critical thickness e_c. The dewetting of a liquid thin film often follows nucleation-and-growth-type dynamics, in which a hole nucleated in the thin film at a certain position grows by spreading radially on the substrate. In this growth process, the velocity at which the hole spreads (V_h) can be expressed by the following equation if the relationship $\theta \ll 1$ rad and $e \ll e_c$ is valid[29]:

$$V_h = \frac{V^*}{6\ln{(l_2/a)}} \theta^3 \qquad (S6).$$

Here, l_2 is the size of the marginal swelling around the hole (Figure S8 **C**). This equation indicates that the characteristic velocity of a liquid can be determined if the spreading velocity of the nucleation-and-growth-type dewetting and the wetting angle of the liquid on the substrate can both be obtained.

Our *in situ* observations succeeded in capturing the nucleation-and-growth-type dewetting dynamics of HDUW at the water–ice III interface (Figures S8 **A** and **B** and SI Movie S5). These observations were performed at –19 ±1 °C by using a differential-interference contrast microscope (the conditions for two-phase coexistence of water and ice III are –20 °C and 248 MPa [(21)]). Immediately after the crystal growth of ice III by pressurization (accompanied by the formation of a macroscopically smooth HDUW–water interface), a hole nucleated in the HDUW thin film on ice III, and grew by spreading radially over the ice surface. The observed dynamics were probably due to the formation of a thin layer of HDUW with a thickness below the critical thickness, as a result of the pressurization. By fitting the time dependence of the radius of the hole, r, using a linear function (Figure S8 **D**), the spreading velocity was determined to be about 7.4 μm/s.

The wetting angle of the thin layer of HDUW was determined by analysing the shift in the interference fringes in the *in situ* interferogram (Figure S9). HDUW was observed by using the interferometer (see Materials and Methods) instead of a differential-interference contrast microscope. Other experimental conditions were the same as those for the observation of the LDUW. Figure S9 **A** is bright-field image without an interferogram, showing an ice III single crystal exhibiting three types of face: I, II, and III (Figure S9 **A**; right). The observations by interferometer were performed for the hole in the HDUW that

appeared on face II, because face II was well developed and parallel to the roof face of the anvil, which played the role of the reference mirror for the interferometer (Figure S9 **B**). As shown in the schematic representation of the optical path in Figure S9 **B**, two types of interference fringe can be generated for the cases with or without a thin layer of HDUW, respectively; the optical paths for these are indicated by the pink and green solid arrows, respectively. The difference between the two optical paths is equal to the thickness of the thin layer of HDUW. The interference fringes appear as parallel and equally spaced straight lines on the flat interface. Therefore, both optical paths reflected on the bulk water–ice III interface and a bulk water/HDUW interface produced parallel and equally spaced straight-line interference patterns. On the other hand, the interference fringes crossing the boundary between the region with and that without an HDUW thin layer, were horizontally shifted at the boundary because of the small difference in the length of the optical paths. The relationship of the thickness of the thin layer, Δe, and the shift in the interference fringe from the straight lines of interference fringes on the reference surface (the bulk water–ice III interface), equal to Δl in our experimental situation, can be expressed as follows[45]:

$$\Delta e = \frac{\lambda}{2 n_w} \cdot \frac{\Delta l}{l_0} \qquad (S7).$$

here, l_0 is the interval between the straight lines of the interference fringes on the reference interface. Therefore, an analysis of the horizontal shift of the interference fringes allowed us to determine the thickness of the thin layer. Figure S9 **C** shows the *in situ* interferograms in which a horizontal shift of the interference fringes was successfully observed. Figure S9 **D** is a magnified image of the interferogram. The horizontal shift can be observed at the boundary between the region where there was a hole and the HDUW thin layer. From these observations, the thickness of the thin layer was estimated to be about 100 nm by using the value of n_W at –20 °C and 248 MPa estimated by the method discussed in the Supplementary Text S4. The estimated value of n_W was 1.377, which is a reasonable value, as the refractive index of ice III at –20 °C and 250 MPa has been estimated to be 1.388 at $\lambda = 514.5$ nm[(40)]. The interferogram indicates that a distance of about 6 μm is required to cross the boundary between the region with the HDUW thin layer to that without such a layer, suggesting that there is a slope with a height increment of 100 nm over the 6 μm distance. Therefore, the wetting angle of the HDUW can be estimated to be about 0.96° (0.017 rad) by considering its tangent. Strictly speaking, the estimated wetting angle is a dynamic wetting angle, θ_D, because the contact line was moving during the observations; however, we assumed that this dynamic wetting angle is equal to the wetting angle. Because Figure S9 **B** suggests that the value of l_2 is about 10 μm, the characteristic velocity of the HDUW can be estimated to be about 100 m/s from Eq. S6.
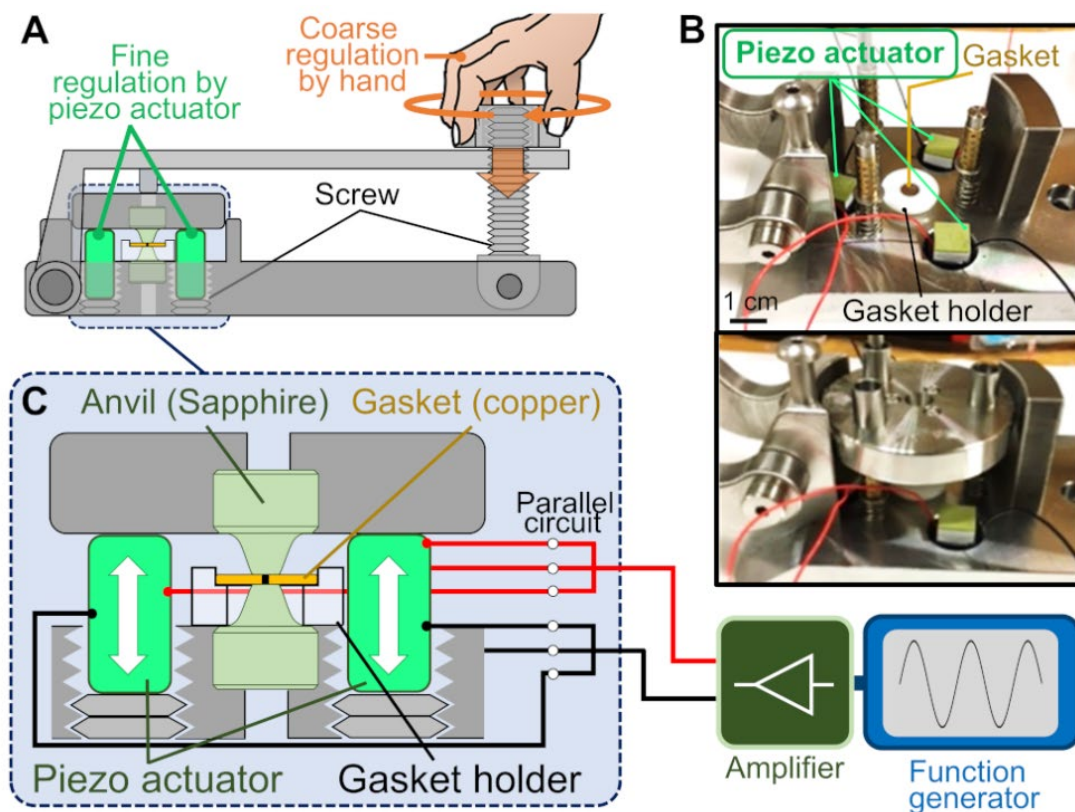
Figure S1. Electrically regulated anvil cell with piezo actuator, dynamic sapphire anvil cell (d-SAC). (A) Schematic overview of the d-SAC. The pressure can be roughly adjusted by manually tightening the screw. The preparation of a single crystal of ice I_h and presetting of the pressure before the observations were carried out by this rough regulation. Subsequent fine regulation of the pressure for the observations was conducted by using the three electrically driven piezo actuators. **(B)** Bird's-eye view of the metal jig supporting the lower anvil (upper) and view after setting the jig supporting the upper anvil (lower). The lower jig has three holes to contain the piezo actuators at intervals of 120° with the anvil at the centre. **(C)** The magnified schematic of the region highlighted in blue in schematic A. The three piezo actuators are connected through a parallel circuit to the function generator as the electrical source and an amplifier as the piezo controller.
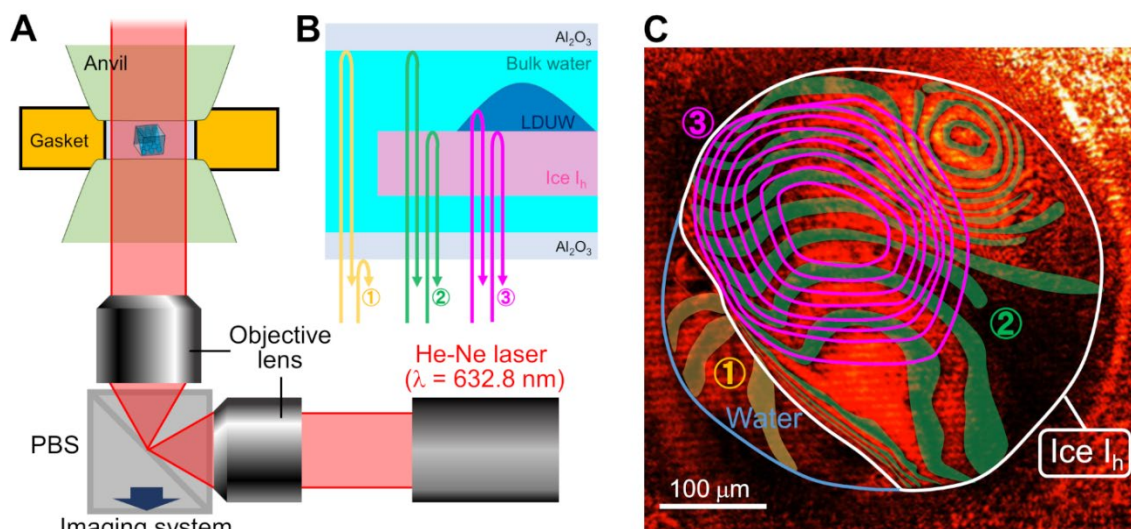
Figure S2. Experimental setup of the microinterferometer and *in situ* observation of the thin layer of LDUW at the water–growing ice interface with the microinterferometer. (**A**) Schematic representation of the microinterferometer. (**B**) Conceivable optical paths that could give rise to the three kinds of interference fringes seen during the *in situ* observations: (1) interference between light reflected by the air–anvil interface at the bottom and light reflected by the bulk water–anvil interface at the top (yellow); (2) interference between light reflected by the upper bulk water/anvil interface and light reflected by the ice crystal–bulk water interface (green); and (3) interference between light reflected by the upper bulk water–anvil interface and that reflected by the LDUW–bulk water interface (magenta). (**C**) An example of a microinterferogram that shows each of the three types of interference fringe. Each of the three kinds of interference fringe is highlighted in the corresponding colour indicated in B and denoted by the corresponding number. The region outlined by the solid white line indicates a single crystal of ice. The region outlined by the solid cyan line indicates a region of water without an ice crystal. See also SI Movie S2.
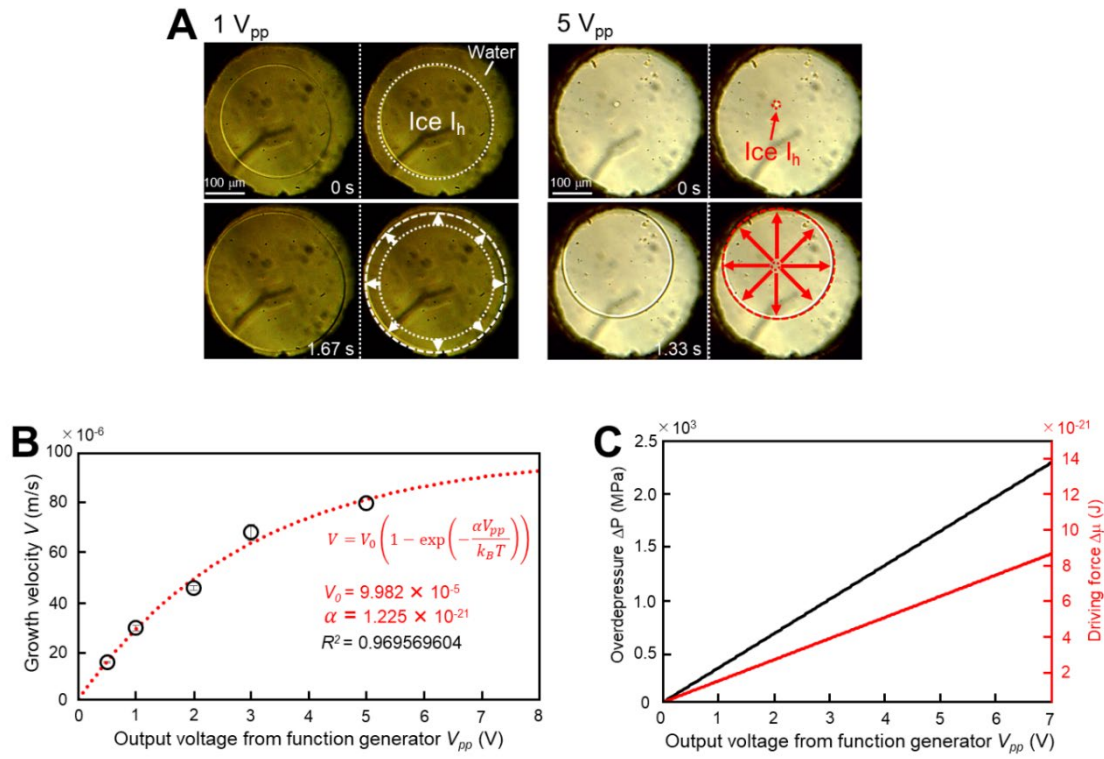
Figure S3. Estimation of the effective overdepressure at the water–ice I_h interface and the thermodynamic driving force for crystallization produced by the actuating d-SAC. (**A**) Timelapse in situ micrographs showing the dynamics of crystal growth of a single crystal of ice I_h driven by depressurization using the d-SAC. The left and right micrographs are for output voltages (V_{pp}) of 1 and 5 V, respectively, from the function generator. (**B**) The dependence of the crystal-growth velocity of ice I_h on the output voltage. The black circles indicate measured values. The red dotted line indicates the fitting curve for Eq. S1. The values shown in the graph are the values of the kinetic coefficient, the constant that links the output voltage with the thermodynamic driving force, and the determination coefficient R^2. (**C**) Dependence of the effective overdepressure at the water–ice interface and the thermodynamic driving force for crystallization.

$$\tan\theta = \frac{d_2 - d_1}{L}$$

$$d_2 - d_1 = \frac{\lambda}{2n_L}$$

$n_W > n_L > n_I$

Bulk Water (n_W)

LDUW (n_L)

$d_2 - d_1$

d_2

L

d_1

θ

Ice I$_h$ (n_I)

$2n_L d_1 = m\lambda$

$2n_L d_2 = (m+1)\lambda$

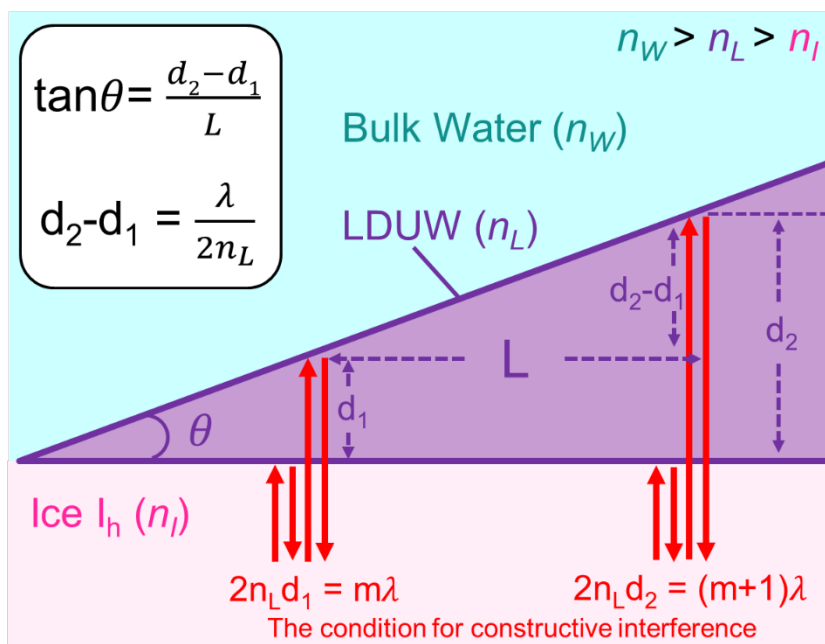The condition for constructive interference

Figure S4. Schematic showing the relationship of the wetting angle of LDUW at the water–ice I$_h$ interface, based on the interval of the interference fringes in the *in situ* microinterferograms. The pink, purple, and light-blue regions represent ice I$_h$, LDUW, and bulk water, respectively, and their refractive indices are represented as n_I, n_L and n_W, respectively. The red arrows indicate the optical paths that give rise to the mth and $(m + 1)^{th}$ constructive interferences. The wetting angle is θ. The distance between the mth and $(m + 1)^{th}$ interference fringes is indicated as L. The thicknesses of LDUW where the mth and $(m + 1)^{th}$ interference fringes are generated are indicated as d_1 and d_2, respectively.
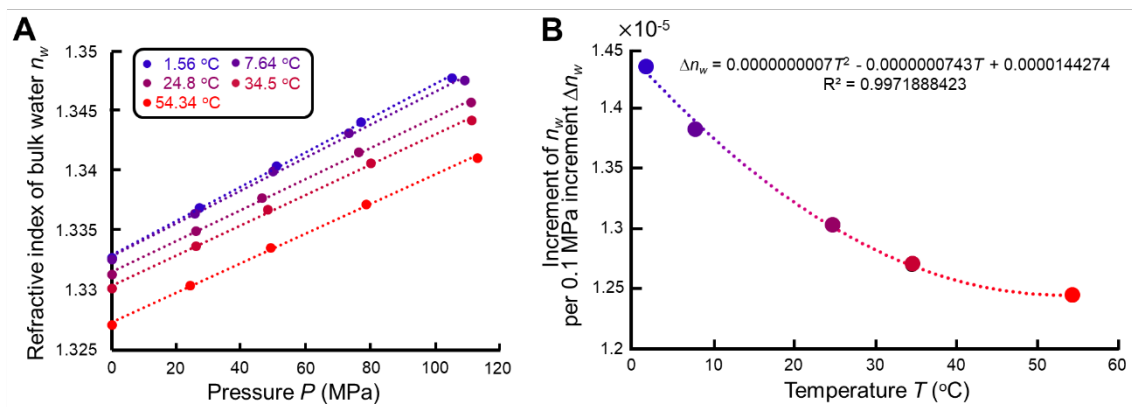
Figure S5. Pressure dependence of the refractive index of bulk water at 643.847 nm, as provided by Cho *et al.*[38], and the temperature dependence of the increment of the refractive index per 0.1 MPa of pressure increment (Δnw). (A) Pressure dependences of the refractive index of bulk water at 1.56, 7.64, 24.8, 34.5, and 54.34 °C and 643.847 nm, as provided by Cho *et al.*[38]. The circles coloured in blue, purple, reddish-purple, reddish-brown, and red are the data points at 1.56, 7.64, 24.8, 34.5 and 54.34 °C, respectively. The dotted lines are the fitting linear lines we used to obtain the Δn_W value at each temperature shown in **B**. **(B)** Temperature dependence of the increment of the refractive index per 0.1 MPa of pressure increment, based on the analysis in **A**. The colours of the circles correspond to those indicated in **A**. The dotted line is the fitting curve obtained by using a quadratic polynomial. The equation represents the fitted curve.
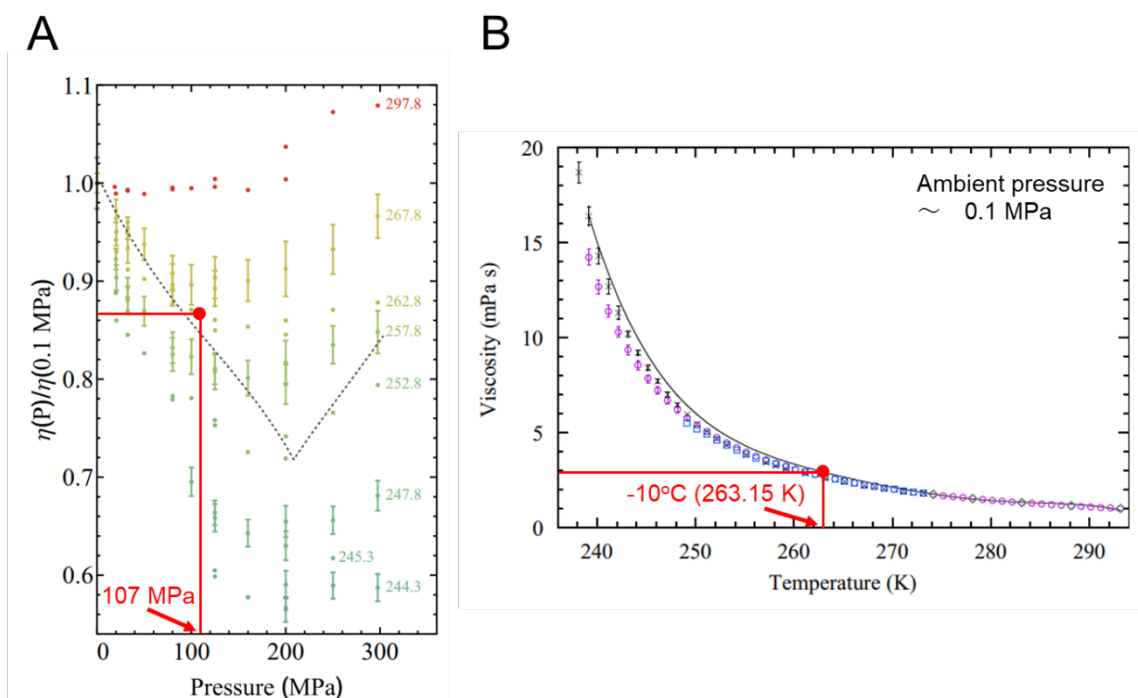
Figure S6. Dependence of the viscosity of bulk water on the pressure and temperature. (**A**) Dependence of the viscosity of bulk water at –28.85 °C (244.3 K), –27.85 °C (245.3 K), –25.35 °C (247.8 K), –20.35 °C (252.8 K), –15.35 °C (257.8 K), –10.35 °C (262.8 K), –5.35 °C (267.8 K), and 24.65 °C (297.8 K) normalized by the viscosity of bulk water at a pressure of 0.1 MPa, as provided by Singh *et al.*[31] The point indicated by the red dot corresponds to the temperature and pressure in our experiments. The grey dotted curve denotes the melting lines of ice I$_h$ and ice III. This graph is adapted from Ref. 31 with the permission of the US National Academy of Sciences (NAS). (**B**) Dependence of viscosity of bulk water on the temperature at a pressure of 0.1 MPa, as provided by Dehaoui *et al.* [32] The point indicated by the red dot is the point used in our estimation. This graph is adapted from Ref. 32 with the permission of NAS.
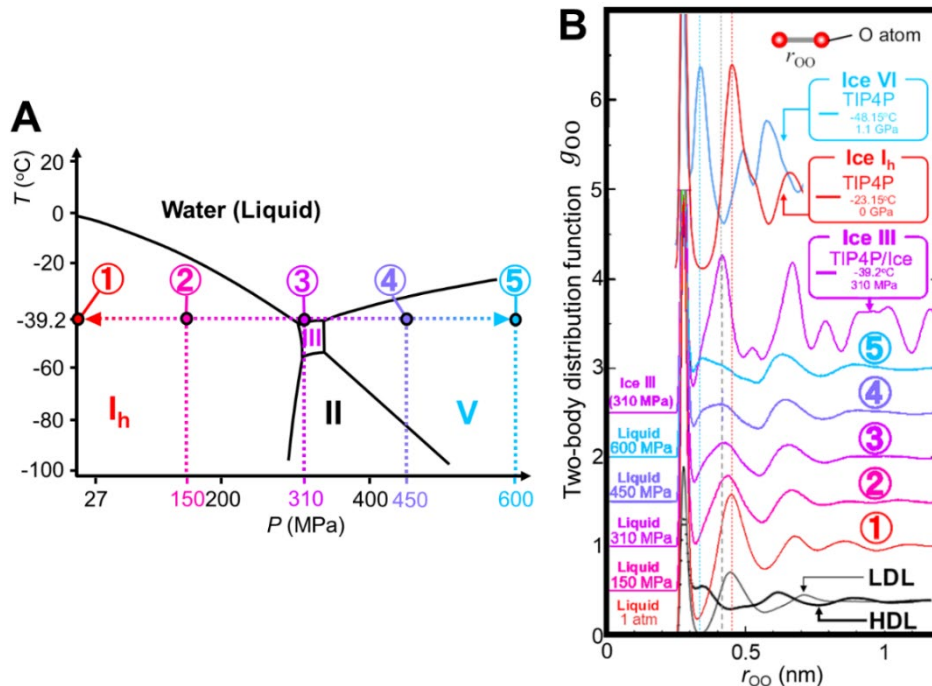
Figure S7. Comparison of oxygen–oxygen two-body distribution functions (TBDFs) for LDL, HDL, Ice I$_h$, Ice III, Ice VI, and supercooled waters under a high pressure. (**A**) Phase diagram of water from molecular-dynamics (MD) simulation using TIP4P/Ice model[35,36], and temperature–pressure conditions in which the MD simulations to provide the TBDFs of the supercooled waters were performed. The TIP4P/Ice model was used for the simulation of supercooled waters at 1 atm, 150 MPa, 310 MPa, 450 MPa, and 600 MPa and –39.2 °C[21], so that the conditions covered a wide range of pressures across the conditions for the coexistence of water and ice III phases. These conditions are denoted by the numbers 1 to 6, respectively. (**B**) Comparison of the TBDFs: The TBDFs of LDL and HDL, indicated by thin and thick solid black lines, respectively, are those obtained by Soper *et al.* using a combination of the results of neutron-diffraction experiments at –5.15 °C and pressures of 26, 209 and 400 MPa and the results of an empirical potential structure refinement simulation[19]. The TBDFs of the supercooled waters obtained by simulation with the TIP4P/Ice model are shown by the solid lines indicated by the corresponding numbers to those indicated in **A**. The change in these TBDFs from an LDL-like to an HDL-like local structure with increasing pressure supports the dynamic crossover from an LDL-like to an HDL-like water above the melting temperature. The TBDF of ice I$_h$ provided by the MD simulation using the TIP4P model at –23.15 °C and 0 GPa[33] is indicated by the unnumbered solid red line. The TBDF of ice I$_h$ is similar to those of LDL and the supercooled liquid numbered 1. The TBDF of ice VI simulated by the MD simulation using TIP4P model at –48.15 °C and 1.1 GPa is indicated by unnumbered solid cyan line[33]. The TBDF of ice VI is similar to those of HDL and the supercooled liquid numbered 5. The TBDF of ice III provided by the MD simulation using TIP4P/Ice model is shown by the unnumbered solid purple line[21]. The TBDF of ice III is similar to that of the supercooled water numbered 3, the local structure of which is similar to that of an intermediate between LDL and HDL. The vertical red, grey, and cyan broken lines indicate

the positions of the TBDF second peaks of ice I_h, ice III, and ice VI, respectively to serve as eye guides for comparing the TBDFs.
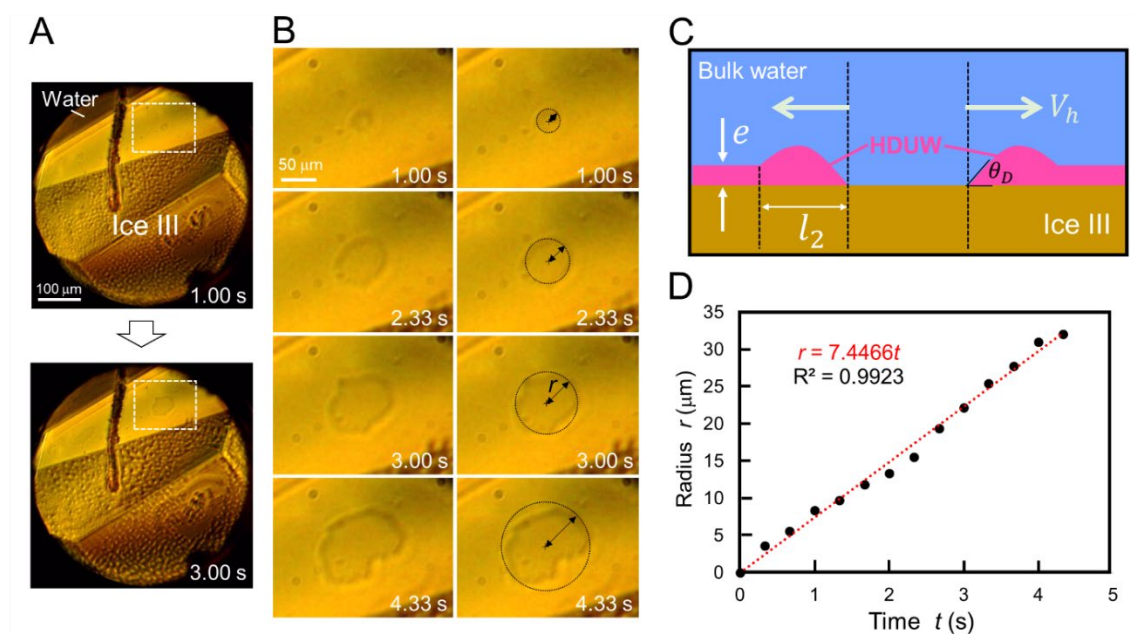
Figure S8. Analysis of nucleation-and-growth-type dewetting dynamics of HDUW at the water–ice III interface. (**A**) Time-lapse *in situ* optical micrographs showing the relaxation process of the water–ice III interface from the nonequilibrium state immediately after rapid pressurization by the d-SAC. (**B**) Time-lapse micrographs without (left) and with (right) eye guides showing the nucleation-and-growth-type dewetting dynamics of the HDUW, which took place in the region indicated by the dashed square in **A** after pressurization. The black dotted circle of radius r, denoted by the black arrow, indicates the hole in the HDUW resulting from dewetting. Although the hole was not completely circular in the later stages of the dynamics, for the sake of simplicity we measured its radius as that of a complete circle, regarding the longest distance from the centre of the hole to the front line of the dewetting as the radius of the circle. (**C**) Schematic showing a simplified model of the cross-section of the HDUW thin layer and ice III when nucleation-and-growth-dewetting dynamics occur. (**D**) Dependence of the radius of the hole in the HDUW on time. The black points indicate the measured radius at each time. the red dotted line is the result of linear fitting. The fitting function is indicated in red. See also SI Movie S5.
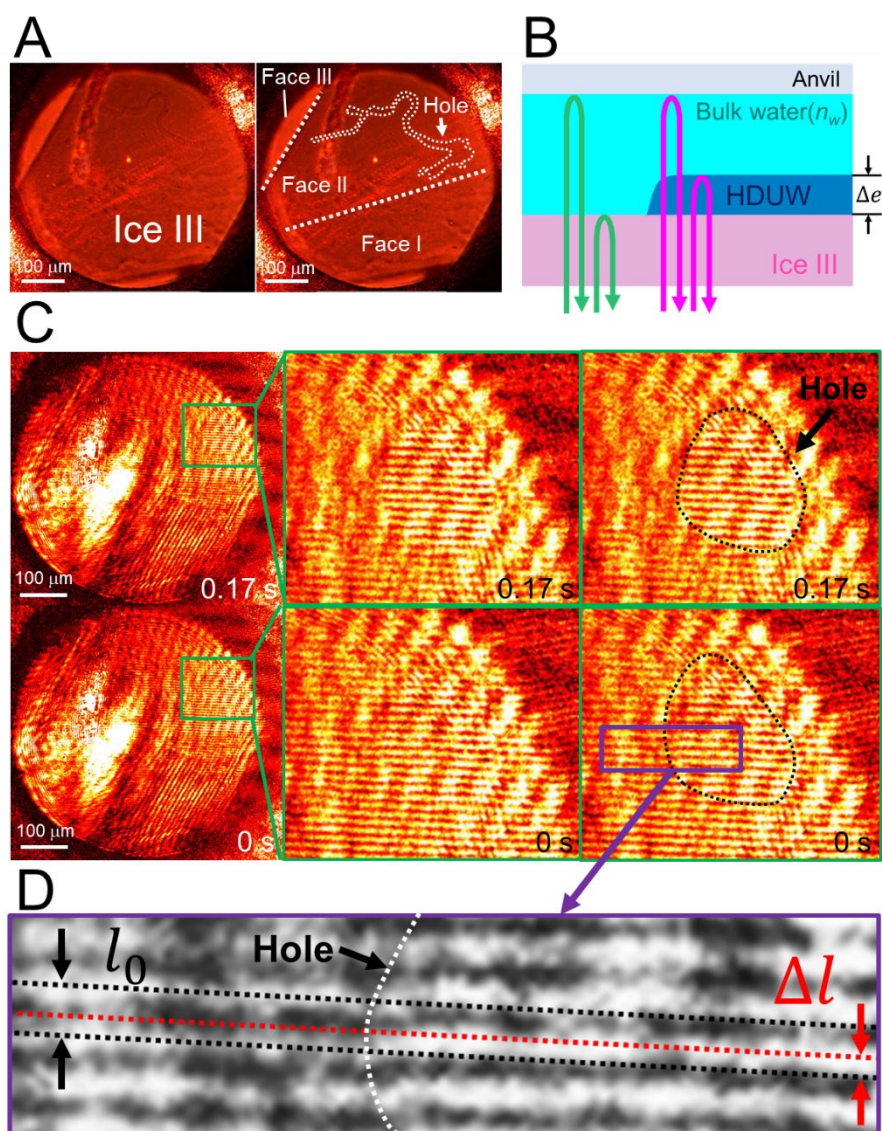
Figure S9. *In situ* **microinterferogram of the hole in the HDUW thin layer at the water–ice III interface.** (**A**) Bright-field micrographs showing the water–ice III interface at which the interferometric observations were performed. The right-hand micrograph is the same as the left-hand one, but with eye guides. The ice III crystal showed three difference faces: faces I, II, and III. The hole that appeared on face III, outlined by the white dotted line in this micrograph, was observed by *in situ* interferometry. (**B**) Schematic illustration showing the two possible optical paths that could give rise to the observed interference fringes, indicated by green and pink arrows, respectively. The optical path indicated by the green arrows involves interference between light reflected by the bulk water–anvil interface and that reflected by the bulk water–ice III interface. The path indicated by the pink arrows shows the interference between the light reflected by the bulk water–anvil interface and that reflected by the bulk water–HDUW interface. These optical

paths practically correspond to that of a Michelson-type interferometer, with the bulk water/anvil interface acting as a reference mirror, giving interference fringes with parallel and equally spaced straight lines. The small difference in height between the interface with and without the HDUW thin layer (Δe) causes a shift in the interference fringes when one crosses the boundary from the region with a HDUW layer to that without such a layer. (**C**) Interferograms showing horizontal shift in the interference fringes. The upper row shows the interferogram in which interference fringes for the bulk water–ice III interface, which correspond to the fringes indicating the hole, are clearly generated. The lower row shows the interferogram with interference fringes of both interfaces shown in green and pink in **B**. The left-hand column contains the interferogram taken by the *in situ* interferometric observations. The middle column shows magnified interferograms of the region delineated by the green squares in the interferograms in the left-hand column without eye guides. The right-hand column shows magnified interferograms with eye guides to indicate the hole. (**D**) Magnified interferograms of the region indicated by the purple square in the lower-right-hand micrograph in **C**. A horizontal shift in the interference fringe, denoted Δl, can be observed at the boundary between the hole and HDUW layer, as indicated by the white dotted line.

Legends for SI Movies S1–S5

SI Movie S1 (separate file). Appearance of Low-Density Unknown Water at the Interface between Water and Ice I$_h$ Grown by Decompression. The movie Corresponds to Figure 2

SI Movie S2 (separate file). ***In situ* Laser–Interferometric Observation of Low-Density Unknown Water at the Interface between Water and Ice I$_h$ Grown/Melted by De/Compression.** The movie Corresponds to Figure S2.

SI Movie S3 (separate file). Appearance of Low-Density Unknown Water at the Interface between Water and Ice I$_h$ Melted by Compression. The movie Corresponds to Figure 3.

SI Movie S4 (separate file). Coalescence Dynamics of a Low-Density Unknown Water Droplet with Its Thin Layer. The movie Corresponds to Figure 4.

SI Movie S5 (separate file). Nucleation-and-Growth-Type Dewetting Dynamics of High-Density Unknown Water at Water–Ice III Interface. The movie Corresponds to Figure S8.

SI References

38.   Cho, C. H.; Urquidi, J. Mixture model description of the T–P dependence of the refractive index of water. *J. Chem. Phys.* **2001**, 114, 3159–3162.

39.   Robinson, G. W.; Cho, C. H.; Gellene, G. I.; Refractive index mysteries of water. *J. Phys. Chem. B* **2000**, 104, 7179–7182.

40.   Tilton, L. W.; Taylor, J. K. Refractive index and dispersion of distilled water for visible radiation, at temperatures 0 to 60 °C. *J. Res. Natl. Bur. Stand. (U. S.)* **1938**, 20, 419–477.

41.   Sánchez, C. M.; Rubio, G. G.; Mulvaney, P.; Martínez, A. G.; Liz-Marzán, L. M.; Rodríguez, F. Monodisperse gold nanorods for high-pressure refractive index sensing. *J. Phys. Chem. Lett.* **2019**, 10, 1587–1593.

42.   Handel, R.; Davidchack, R. L.; Anwar, J.; Brukhno, A. Direct calculation of solid–liquid interfacial free energy for molecular systems: TIP4P ice–water interface. *Phys. Rev. Lett.* **2008**, 100, 036104.

43.   Ludlam, F. H.; Mason, B. J.; *The physics of clouds. in Geophysik II/Geophysics II. Handbuch der Physik/Encyclopedia of Physics*, *Vol. 10.*; Bartels, J., Ed.; Springer: Swizerland, 1957.

44.   Turnbull, D. Formation of crystal nuclei in liquid metals. *J. App. Phys.* **1950**, 21, 1022–1028.

45.   Nagashima, K.; Maurais, J.; Murata, K.; Furukawa, Y.; Ayotte, P.; Sazaki, G. Appearance and disappearance of quasi-liquid layers on ice crystals in the presence of nitric acid gas. *Crystals* **2020**, 10, 72.